














# Ammonia Emission in Various Star-forming Environments: A Pilot Study of Planck Galactic Cold Clumps

O. Fehér<sup>1</sup> , L. Viktor Tóth<sup>2</sup>, Alex Kraus<sup>3</sup> , Rebeka Bógnér<sup>2</sup>, Gwanjeong Kim<sup>4</sup>, Tie Liu<sup>5</sup> , Ken'ichi Tatematsu<sup>4,6</sup> , Victor Tóth<sup>2,7</sup>, David J. Eden<sup>2,7</sup> , Naomi Hirano<sup>8</sup> , Mika Juvela<sup>9</sup> , Kee-Tae Kim<sup>10,11</sup> , Di Li<sup>12,13,14</sup> , Sheng-Yuan Liu<sup>8</sup> , and Yuefang Wu<sup>15,16</sup> 

The TOP-SCOPE Collaboration

<sup>1</sup> Institut de Radioastronomie Millimétrique, 300 Rue de la Piscine, F-38406, Saint Martin d'Hères, France; [feher@iram.fr](mailto:feher@iram.fr)

<sup>2</sup> Eötvös Loránd University, Department of Astronomy, Pázmány Péter sétány 1/A, 1117 Budapest, Hungary

<sup>3</sup> Max-Planck-Institut für Radioastronomie, Auf dem Hügel 69, D-53121 Bonn, Germany

<sup>4</sup> Nobeyama Radio Observatory, National Astronomical Observatory of Japan, National Institutes of Natural Sciences, Nobeyama, Minamimaki, Minamisaku, Nagano 384-1305, Japan

<sup>5</sup> Shanghai Astronomical Observatory, Chinese Academy of Sciences, 80 Nandan Road, Shanghai 200030, People's Republic of China

<sup>6</sup> Department of Astronomical Science, SOKENDAI, 2-21-1 Osawa, Mitaka, Tokyo 181-8588, Japan

<sup>7</sup> Astrophysics Research Institute, Liverpool John Moores University, IC2, Liverpool Science Park, 146 Brownlow Hill, Liverpool, UK

<sup>8</sup> Academia Sinica, Institute of Astronomy and Astrophysics, 11F of Astronomy-Mathematics Building, AS/NTU No. 1, Sec. 4, Roosevelt Rd., Taipei 10617, Taiwan, R.O.C.

<sup>9</sup> Department of Physics, PO Box 64, University of Helsinki, 00014, Helsinki, Finland

<sup>10</sup> Korea Astronomy and Space Science Institute, 776 Daedeokdaero, Yuseong-gu, Daejeon 34055, Republic of Korea

<sup>11</sup> University of Science & Technology, 176 Gajeong-dong, Yuseong-gu, Daejeon, Republic of Korea

<sup>12</sup> National Astronomical Observatories, Chinese Academy of Sciences, Beijing 100101, People's Republic of China

<sup>13</sup> Key Laboratory of FAST, National Astronomical Observatories, Chinese Academy of Sciences, Beijing 100101, People's Republic of China

<sup>14</sup> School of Astronomy and Space Science, University of Chinese Academy of Sciences, Beijing 101408, People's Republic of China

<sup>15</sup> Department of Astronomy, School of Physics, Peking University, Beijing 100871, People's Republic of China

<sup>16</sup> Kavli Institute for Astronomy and Astrophysics, Peking University, Beijing 100871, People's Republic of China

Received 2020 December 17; revised 2021 September 28; accepted 2021 September 29; published 2022 January 12

## Abstract

The Planck Catalogue of Galactic Cold Clumps provides an all-sky sample of potential star-forming regions based on the submillimeter emission of their dust content. Around 1000 of these Planck objects were mapped with the James Clerk Maxwell telescope in the submillimeter range during the SCOPE survey, identifying prestellar and protostellar dense clumps inside them. We used the Effelsberg 100 m telescope to observe the emission lines of the NH<sub>3</sub> inversion transitions toward a sample of 97 dense objects in varying environments in order to assess the physical parameters of their gas content. We derive their temperature, density, and velocity dispersion, correlating the resulting parameters with the environmental and evolutionary characteristics of the targets and with regard to their distance and physical size. We examine the dependence of physical parameters on distance and Galactic position and compare the gas-based and dust-continuum-based temperatures and densities. Together with the presence of maser emission and higher inversion transitions of ammonia, we may differentiate between certain groups of targets, e.g., filamentary, protostellar clumps, and high-latitude, core-sized, starless sources.

*Unified Astronomy Thesaurus concepts:* [Interstellar molecules \(849\)](#); [Dense interstellar clouds \(371\)](#); [Star formation \(1569\)](#); [Dust continuum emission \(412\)](#); [Interstellar medium \(847\)](#); [Protostars \(1302\)](#); [Molecular clouds \(1072\)](#)

*Supporting material:* figure sets, machine-readable tables

## 1. Introduction

The initial conditions inside star-forming clouds determine the number and parameters of the stars forming in it (Bergin 2007). In order to follow the formation and evolution of star-forming sites and disentangle the complex interplay of gravitational collapse, turbulence, fragmentation, magnetic field, and environmental effects during early star formation, a large sample of cloud cores need to be examined in a multiscale and multiwavelength manner.

A catalog of more than 13,000 Planck Galactic Cold Clumps (PGCCs) was released (Planck Collaboration XXXVIII 2016)

based on the all-sky survey of the Planck telescope at submillimeter wavelengths, providing a heterogeneous sample of cold and dense, possibly star-forming regions throughout the Galaxy. According to the Planck data, the objects show temperatures of  $T = 6\text{--}20$  K and hydrogen column densities of  $N(\text{H}_2) = 10^{20}\text{--}10^{23}$  cm<sup>-2</sup>, with sizes ranging from 0.1 pc to over 10 pc and masses from below  $0.1 M_{\odot}$  to over  $10^4 M_{\odot}$ . Several studies have been made to investigate the morphology, dust properties, and the characteristics and kinematics of the gas content in subsets of the Planck catalog (Juvela et al. 2012b; Wu et al. 2012; Meng et al. 2013; Montillaud et al. 2015; Juvela et al. 2015a, 2015b) or of well-known complex molecular regions in the framework of these new data, like the Heiles Cloud 2 (Tóth et al. 2004; Fehér et al. 2016).

Two large projects were executed to systematically study these regions as well: the TRA0 Observations of PGCCs



Original content from this work may be used under the terms of the [Creative Commons Attribution 4.0 licence](#). Any further distribution of this work must maintain attribution to the author(s) and the title of the work, journal citation and DOI.

(TOP) with the 14 m telescope of the Taeduk Radio Astronomy Observatory (TRAO) mapped the  $J = 1-0$  transitions of  $^{12}\text{CO}$  and  $^{13}\text{CO}$  toward 2000 PGCCs, and the SCUBA-2 Continuum Observations of Pre-protostellar Evolution (SCOPE) with the James Clerk Maxwell telescope (JCMT) surveyed the 850  $\mu\text{m}$  continuum emission of more than 1000 PGCCs selected from the TOP sample (Liu et al. 2018). The SCOPE results show that most of the PGCCs have significant substructures: the 4000 dense objects identified inside them are the prime candidates to examine the very early phases of star formation, how low- and high-mass prestellar and protostellar cores form and evolve, and how the physical and chemical properties of cores can vary in different environments (Eden et al. 2019). Follow-up observations of the emission of several molecular transitions toward subsets of the SCOPE objects were performed using the SMT 10 m, SMA, NRO 45 m, and KVN 21 m telescopes and the Atacama Large Millimeter/submillimeter Array (Liu et al. 2016, 2018; Kim et al. 2020; Tatematsu et al. 2017, 2020).

A sample of 97 dense objects was compiled specifically for pilot studies of PGCCs located in different environments. The targets were classified after visual inspection of the SCUBA-2 maps into three environmental categories: 35 high-latitude isolated sources or small clusters, 49 sources in filaments, and 13 clusters close to the Galactic plane. These objects may include both close-by, small cores and distant, larger clumps and clouds. The targets were observed using the NRO 45 m and the JCMT telescopes, detecting several molecular species, submillimeter, and far-infrared continuum (Kim et al. 2020). To complement these projects, we observed the  $\text{NH}_3(1, 1)$ , (2, 2), and (3, 3) inversion transitions toward these objects using the Effelsberg 100 m telescope. At the same time, thanks to the subband setup of the 1.3 cm receiver, we were able to detect  $\text{H}_2\text{O}$  maser emission as well at 22.235 GHz.

Ammonia is a reliable tracer of kinetic temperature (Ho & Townes 1983; Juvela et al. 2012a) owing to the fact that the relative populations of its rotational stages characterized by the quantum numbers  $J$  and  $K$  depend only on collisions, since dipole transitions between the different  $K$  ladders are forbidden. The  $(J, K)$  rotational states are divided into inversion doublets, which show hyperfine structure (HFS). These transitions are easily observable from the ground, and the line optical depths can be estimated from the intensity ratio of the hyperfine components. The critical density of the (1, 1) inversion transition is around  $2 \times 10^3 \text{ cm}^{-3}$ ; thus, the line traces the temperature of the dense gas. Our primary goal is to calculate the characteristic temperatures and densities of the SCOPE objects with angular resolution comparable to the dust temperature maps produced by SCUBA-2 and Herschel space observatory.

Table 2 lists the targets, their equatorial coordinates, associations with PGCCs, distances based on the study by Kim et al. (2020), the environmental categories they belong to, and references to previous publications presenting ammonia or water maser observations toward their directions. From the 97 targets on our list, 31 have previous water maser detections and 39 have previous  $\text{NH}_3$  observations. We compare the results derived from these existing  $\text{NH}_3$  data sets and the results of our new study (e.g., spatial and spectral resolution, line velocities, kinetic temperatures, ammonia densities) where it is relevant in Section 3.1.

The study allows us to constrain the physical parameters of the densest regions in the objects and examine these parameters

throughout a diverse sample. The results serve as an input to ongoing chemical evolution studies of starless and star-forming environments, e.g., Tatematsu et al. (2017), who have developed the so-called chemical evolution factor in order to identify cores in the earliest stages of protostellar evolution and on the verge of star formation.

## 2. Observations and Data Analysis

We observed the targets between 2017 February 15 and 18 with the 1.3 cm secondary focus receiver of the Effelsberg 100 m telescope (see Table 2). A bandwidth of 300 MHz was used to measure the three ammonia inversion transitions simultaneously with position switching mode, reaching a spectral resolution of 4.6 kHz that corresponds to  $0.06 \text{ km s}^{-1}$  at the observing frequency of  $\sim 23.7$  GHz. The Effelsberg telescope provides a  $37''$  beam size at this wavelength, the main-beam efficiency was 0.59, and the average system temperature was 85–90 K. We performed observations with a single pointing toward the peaks seen on the SCOPE dust continuum maps with an on-source time of 10–15 minutes; the average resulting rms noise was  $\sigma(T_{\text{MB}}) = 0.12$  K, where  $T_{\text{MB}}$  is the main-beam brightness temperature. Additionally, we aimed to detect  $\text{H}_2\text{O}$  maser emission at 22.235 GHz using the other subband of the receiver.

The calibration and fitting of the spectra were done using the software package CLASS.<sup>17</sup> The raw spectral data were calibrated for atmospheric absorption, and then elevation dependence was corrected by observing NGC 7027 every few hours during all observing days and at several elevations. The flux density of NGC 7027 is known from the model by Zijlstra et al. (2008), allowing us to compute its expected  $T_{\text{MB}}$ . Thus, the ratio of the measured  $T_A$  antenna temperature and the calculated  $T_{\text{MB}}$  was determined on each observing day for the spectra of NGC 7027, and then the same ratios were applied to the spectra of the science targets to convert the scale to  $T_{\text{MB}}$ . We note that since NGC 7027 is a compact source, the resulting  $T_{\text{MB}}$  might overestimate the true brightness temperature of the targets.

The  $\text{NH}_3(1, 1)$  and (2, 2) spectra were used to calculate the physical parameters toward the targets. The (1, 1) and (2, 2) lines were fitted with Gaussian functions to derive the  $T_{\text{MB}}(1, 1)$  and  $T_{\text{MB}}(2, 2)$  peak main-beam brightness temperatures,  $v_{\text{LSR}}(1, 1)_g$  and  $v_{\text{LSR}}(2, 2)_g$  velocities in the LSR (local standard of rest), and  $\Delta v_g(1, 1)$  and  $\Delta v_g(2, 2)$  Gaussian line widths. The HFS of the (1, 1) line was also fitted with model spectra to derive  $\tau_m(1, 1)$  main-group opacity and  $\Delta v_{\text{HFS}}(1, 1)$  HFS line widths.

In case the spectra of the target showed two velocity components, the  $\text{NH}_3(1, 1)$  main groups were first fitted by two Gaussians simultaneously. The software CLASS requires initial estimates of line intensity, HFS line width, velocity, and main-group opacity to perform the HFS fitting. We used the  $T_{\text{MB}}(1, 1)$  and  $v_{\text{LSR}}(1, 1)_g$  values from the Gaussian function fitting, 0.1 MHz for  $\Delta v_{\text{HFS}}(1, 1)$ , and 1.0 for  $\tau_m(1, 1)$  as initial parameters for the HFS fitting. None of these parameters were fixed, except in some cases where the line components were sufficiently blended and could not be otherwise distinguished. In these cases, the  $v_{\text{LSR}}(1, 1)_g$  values were fixed. The  $\text{NH}_3(2, 2)$  line components were also fitted with two Gaussians. Here the initial parameters were the  $v_{\text{LSR}}$  values from the  $\text{NH}_3(1, 1)$  Gaussian fits, the value of  $T_{\text{MB}}(2, 2)$  estimated from the

<sup>17</sup> <http://www.iram.fr/IRAMFR/GILDAS>

spectrum plots, and an estimate of  $1 \text{ km s}^{-1}$  for  $\Delta v_g(2, 2)$ . We did not fix any of these parameters since the volume of material emitting in the (1, 1) and (2, 2) transitions might be different in interstellar clouds. In two cases, multiple velocity components (MVCs) were observed in the (1, 1) transitions but could not be fitted for the (2, 2) lines (targets 69 and 70). Here the  $T_{\text{MB}}$  of the nondetected (2, 2) velocity component was estimated with the  $3\sigma$  value to give an upper limit for the line intensity in the physical parameter calculations.

The detected maser spectra are plotted in Figure 8, while Figure 10 shows the observed  $\text{NH}_3$  spectra toward the targets and the fitted Gaussian and HFS profiles. Table 3 lists the parameters of the fitted Gaussians and HFS profiles. The table also indicates where  $\text{NH}_3(3, 3)$  lines or water masers were detected.

We derive the  $T_{\text{ex}}$  excitation temperature of the  $\text{NH}_3(1, 1)$  transition using the radiative transfer equation

$$T_{\text{MB}}(1, 1) = \frac{h\nu_{11}}{k} [F(T_{\text{ex}}) - F(T_{\text{bg}})] (1 - e^{-\tau_m(1,1)}), \quad (1)$$

where  $\nu_{11}$  is the frequency of the (1, 1) transition,  $T_{\text{bg}}$  is the cosmic background temperature,  $F(T) = 1/(e^{h\nu_{11}/kT} - 1)$ , and we assume local thermodynamic equilibrium and a beam filling factor of 1, which is correct if the targets are larger than the telescope beam.

The  $T_{\text{rot}}$  rotation temperature of  $\text{NH}_3$  can be calculated from the observed  $T_{\text{MB}}$  values of the (1, 1) and (2, 2) transitions (Ho & Townes 1983):

$$T_{\text{rot}} = \frac{-41.5}{\ln\left(\frac{-0.282}{\tau_m(1,1)} \ln\left(1 - \frac{T_{\text{MB}}(2,2)}{T_{\text{MB}}(1,1)} (1 - e^{-\tau_m(1,1)})\right)\right)}. \quad (2)$$

The column density of the ammonia molecules in the upper level can be determined by the equation

$$N_u = \frac{8\pi\nu_{11}^3}{c^3 A} F(T_{\text{ex}}) \int \tau_m(1, 1)(v) dv, \quad (3)$$

where  $A$  is the Einstein coefficient of the  $\text{NH}_3(1, 1)$  transition ( $1.7 \times 10^{-7} \text{ s}^{-1}$ ; Harju et al. 1993). Assuming a Gaussian line profile and integrating  $\tau_m(1, 1)$  over the main line group, we can write the integral as

$$\int \tau_m(1, 1)(v) dv = \frac{\sqrt{\pi}}{2\sqrt{\ln 2}} \Delta v_g(1, 1) \tau_m(1, 1). \quad (4)$$

The  $N(\text{NH}_3(1, 1))$  total column density of the  $\text{NH}_3$  molecules in the (1, 1) state is

$$\begin{aligned} N(\text{NH}_3(1, 1)) &= N_u(1, 1) + N_l(1, 1) \\ &= N_u(1, 1) (1 + e^{h\nu_{11}/kT_{\text{ex}}}). \end{aligned} \quad (5)$$

Ammonia has two species, the ortho- $\text{NH}_3$  ( $K = 3n$ ) and the para- $\text{NH}_3$  ( $K \neq 3n$ ), which arise from the different relative orientations of the three hydrogen spins. Since the higher energy levels are by orders of magnitude less populated on temperatures around 10 K, we may estimate the  $N(\text{NH}_3)$  total para-ammonia column density from the observed (1, 1) and (2, 2) transitions with

$$N(\text{NH}_3) = N(\text{NH}_3(1, 1)) \left(1 + \frac{5}{3} e^{-41.5/T_{\text{rot}}}\right). \quad (6)$$

The  $T_{\text{kin}}$  kinetic temperature of the gas was calculated with the half-empiric equation by Tafalla et al. (2004),

$$T_{\text{kin}} = \frac{T_{\text{rot}}}{1 - \frac{T_{\text{rot}}}{42} \ln(1 + 1.1e^{-16/T_{\text{rot}}})}, \quad (7)$$

and the  $n(\text{H}_2)$  local molecular hydrogen volume density was estimated using the equation by Ho & Townes (1983),

$$n(\text{H}_2) = \frac{A F(T_{\text{ex}}) - F(T_{\text{bg}})}{C F(T_{\text{kin}}) - F(T_{\text{ex}})} [1 + F(T_{\text{kin}})], \quad (8)$$

where  $C$  is the collisional de-excitation rate ( $8.5 \times 10^{-11} \text{ cm}^3 \text{ s}^{-1}$ ; Danby et al. 1988).

Table 4 lists the physical parameters calculated for the targets using Equations (1)–(8). In the case of spectra with MVCs the parameters were computed for all components. The error bars on the various physical parameters were computed by propagating the errors that appear on the line parameters resulting from the least-squares fitting of Gaussian and HFS models to the spectra.

To identify targets emitting on shorter wavelengths, i.e., where star formation might have already started, we used the three shortest-wavelength maps from the Spitzer IRAC instrument (3.6, 4.5, and 5.8  $\mu\text{m}$ ; Werner et al. 2004) where available, and for the rest, the three shortest-wavelength maps by WISE (3.4, 4.6, and 12.1  $\mu\text{m}$ ; Wright et al. 2010). The SIMBAD database (Wenger et al. 2000) was used to identify young stellar objects (YSOs) at or inside of a few-arcsecond radius around the coordinates of our sources, and the results were also cross-checked against the catalog assembled by Kim et al. (2020), where all but three of our targets (target 1, 35, and 36) are included. From the 97 sources, 78 have been associated with YSOs, YSO candidates, or infrared sources and thus are “protostellar.” A total of 19 targets have not been associated with infrared point sources, and we refer to these as “starless” (marked with P for protostellar and S for starless in Table 4).

Figure 10 shows the (1, 1), (2, 2), and, when detected, (3, 3) spectra toward all the targets, and Figure 9 shows the respective WISE or Spitzer maps around the targets with the position of the PGCC ellipses and the location of the targets of the  $\text{NH}_3$  observations.

### 3. Results

#### 3.1. Global Statistics

We have detected the  $\text{NH}_3(1, 1)$  and (2, 2) inversion transitions toward most of our targets. The  $\text{NH}_3(2, 2)$  transition was not detected toward targets 6 and 7. The  $\text{NH}_3(1, 1)$  line was only marginally detected for targets 4 and 7: with  $2.1\sigma$  and  $1.3\sigma$ , respectively, with a velocity resolution of  $0.06 \text{ km s}^{-1}$ , and with  $2.8\sigma$  and  $1.7\sigma$ , respectively, if we smooth the spectra to  $0.11 \text{ km s}^{-1}$ . The  $\text{NH}_3(1, 1)$  HFS was not or marginally detected for targets 3, 4, 5, 6, and 7. The low signal-to-noise ratio of these spectra made it difficult to fit the line parameters reliably; thus, targets 3–7 were excluded from further analysis.

The  $\text{NH}_3(3, 3)$  transition was detected toward 25 targets, and the  $\text{H}_2\text{O}$  maser emission was detected toward 21 targets. MVCs were detected and fitted with Gaussian and HFS functions for 27 targets. Additionally, broad or blended velocity components were detected toward targets 29, 30, and 61, where the line shape could not be fitted well; thus, these were excluded from further analysis. Furthermore, due to the often difficult

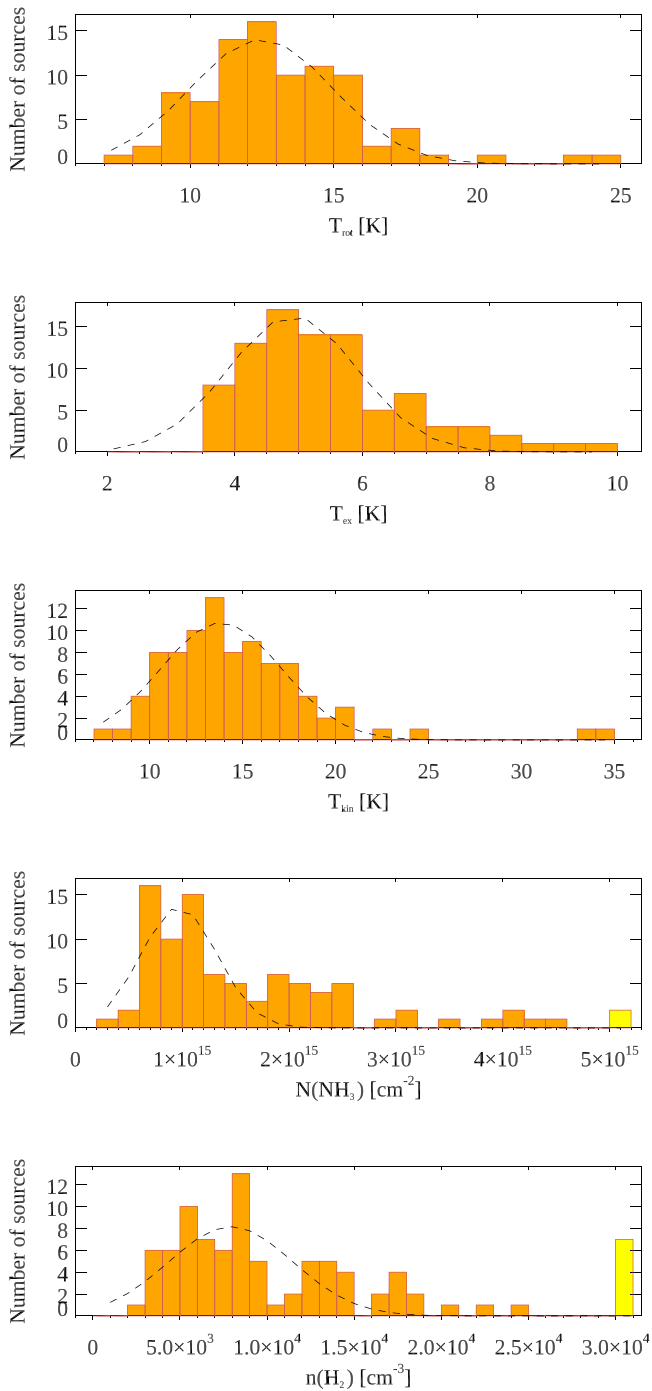


**Figure 1.** Temperature and density histograms of the observed SCOPE targets. The Gaussian functions fitted to the distributions are marked with dashed lines. All values  $N(\text{NH}_3) > 5 \times 10^{15} \text{ cm}^{-2}$  and  $n(\text{H}_2) > 3 \times 10^4 \text{ cm}^{-3}$  are indicated with yellow bins.

separation of MVCs, velocity dispersion statistics is only provided for targets with only one  $\text{NH}_3$  velocity component.

Figure 1 shows the distribution of the sources according to their kinetic, excitation, and rotation temperatures;  $\text{NH}_3$  column density; and  $\text{H}_2$  volume density. The rotation and excitation temperatures vary in the range of 7.8–24.2 K and 3.6–9.6 K, respectively, and the average kinetic temperature is 14.7 K, with values between 8 and 35 K. As the Gaussian functions fitted to these distributions show, 68% of the sources fall in the range of  $T_{\text{rot}} = 10\text{--}14.8 \text{ K}$ ,  $T_{\text{ex}} = 4.2\text{--}5.8 \text{ K}$ , and

$T_{\text{kin}} = 10.3\text{--}16.6 \text{ K}$ . The coldest sources are target 8 with  $T_{\text{kin}} = 8 \text{ K}$ , an isolated, starless, high-density source that appears as a very small object on the SCUBA-2 map; target 86 with  $T_{\text{kin}} = 9 \text{ K}$ ; and target 2 with  $T_{\text{kin}} = 10 \text{ K}$ , which is also starless and has the highest  $\text{H}_2$  volume density in the sample with  $3.6 \times 10^5 \text{ cm}^{-3}$ . The coldest filament is G82.39–1.84, which contains low-temperature SCOPE objects (targets 59–62) with fairly high volume densities:  $T_{\text{kin}} = 9\text{--}10 \text{ K}$  and  $n(\text{H}_2) \sim 10^4 \text{ cm}^{-3}$ . The warmest source is target 27 in the filament G16.96+0.27, where all SCOPE sources show high kinetic temperatures (17–35 K) and some of them show high  $\text{H}_2$  volume densities. Targets 90, 91, and 92 in the filament G173.12+2.36 also show higher  $T_{\text{kin}}$  than the average, and  $\text{NH}_3(3, 3)$  and  $\text{H}_2\text{O}$  maser were also detected toward them. These are signs of warm, dense material in the early stages of star formation.

The  $\text{NH}_3$  column densities are  $3.4 \times 10^{14}\text{--}1.5 \times 10^{16} \text{ cm}^{-2}$  in the sample, with sources in the interquartile range showing  $5.2 \times 10^{14}\text{--}1.5 \times 10^{15} \text{ cm}^{-2}$ . The  $\text{H}_2$  volume densities are  $2.9 \times 10^3\text{--}3.6 \times 10^5 \text{ cm}^{-3}$ , with sources in the interquartile range showing  $4.2 \times 10^3\text{--}1.1 \times 10^4 \text{ cm}^{-3}$ . The highest  $\text{H}_2$  volume densities belong to three high-latitude objects, targets 2, 8, and 86, all fairly cold. However, the errors of the density values are also very high in these cases; thus, the conclusion regarding high densities is not significant.

We calculated the  $\sigma_{\text{tot}}$  total velocity dispersion using the equation  $\sigma_{\text{tot}} = \frac{\Delta v(1,1)_g}{\sqrt{8 \ln 2}}$  from the line width values listed in Table 3. The  $\sigma_{\text{tot}}$  values are in the range  $0.1\text{--}1.0 \text{ km s}^{-1}$ . The  $\sigma_{\text{th}} = \sqrt{\frac{k_B T_{\text{kin}}}{m_{\text{NH}_3}}}$  thermal velocity dispersion was also calculated, and the values vary between  $0.06$  and  $0.14 \text{ km s}^{-1}$ . We can calculate from this the  $\sigma_{\text{turb}}$  turbulent velocity dispersion as well with the equation  $\sigma_{\text{tot}}^2 = \sigma_{\text{th}}^2 + \sigma_{\text{turb}}^2$ , and the results are between  $0.07$  and  $1.0 \text{ km s}^{-1}$ .

As mentioned before, the detected  $\text{NH}_3$  line parameters and the calculated physical parameters toward the targets were checked against catalogs presenting  $\text{NH}_3$  and water maser studies from previous years. As Table 2 shows, most of our targets are featured in four larger studies by Jijina et al. (1999), Camarata et al. (2015), Svoboda et al. (2016), and Wienen et al. (2012). The data set assembled by Jijina et al. (1999) is itself collected from earlier observations performed with the Effelsberg, Haystack, Green Bank, etc., telescopes, and the data set analyzed by Camarata et al. (2015) is composed of the data presented by Wienen et al. (2012) acquired with the Effelsberg telescope and the observations of the authors with the Parkes telescope. Svoboda et al. (2016) used the Green Bank Telescope.

The results of our survey generally match the ammonia parameters presented in these various studies. The  $v_{\text{LSR}}$  velocities of the detected  $\text{NH}_3(1, 1)$  lines usually match within  $0.5 \text{ km s}^{-1}$ , even though most of the previous studies we reference used lower velocity resolution than our measurements. Another remark is that for most targets where our analysis indicated MVCs, the reference studies do not (e.g., targets 10, 12, 14, 41).

The physical parameters derived from previous observations made by the Effelsberg telescope are in good agreement with our results in most cases. One example is target 8, which was measured by Ungerechts et al. (1980) with close to the same spectral resolution ( $0.08 \text{ km s}^{-1}$ ) and similarly low  $T_{\text{kin}}$  to the current study (7.5 K, which was also the lowest in their

sample). The excitation and rotational temperatures of this source are also close to our results ( $T_{\text{ex}}=6\text{--}8.6\text{ K}$  and  $T_{\text{rot}}=7.5\text{--}10\text{ K}$ ), together with the  $\text{NH}_3$  column densities ( $8 \times 10^{14}\text{--}3 \times 10^{15}\text{ cm}^{-2}$ ).

The parameters reported by Wielen et al. (2012) also using the Effelsberg antenna are generally close to the ones reported here, allowing for differences arising from the lower spectral resolution ( $0.5\text{--}0.7\text{ km s}^{-1}$ ) of the earlier study. Kinetic and rotational temperatures match usually within  $1\text{--}2\text{ K}$  for 8 of the 13 targets (we consider here those where the target position from the literature is close to our target, e.g., the nonstarred references in Column (8) of Table 2). For the rest of the targets, the match is worse, like target 13, where Wielen et al. (2012) measure  $T_{\text{kin}}=17\text{ K}$  versus our  $14\text{ K}$ , but the  $\text{NH}_3$  column densities are close ( $1.6 \times 10^{15}\text{ cm}^{-2}$  vs. our  $1.5 \times 10^{15}\text{ cm}^{-2}$ ). Another example is target 17, where they measure  $T_{\text{kin}}=16.6\text{ K}$ , which is  $4\text{ K}$  higher than our result, and  $N(\text{NH}_3)=2.6 \times 10^{15}\text{ cm}^{-2}$ , which is  $1.8 \times 10^{15}\text{ cm}^{-2}$  lower than our estimate. In case two velocity components were measured in our study but not by Wielen et al. (2012), their results are sometimes close to the average  $T_{\text{kin}}$  and total  $N(\text{NH}_3)$  calculated from our two detected velocity components (e.g., targets 14, 16). Our results generally match the work of other studies using the Effelsberg telescope with lower spectral resolution less well, e.g., Chira et al. (2013) with  $0.38\text{ km s}^{-1}$ , Molinari et al. (1996) with  $0.3\text{ km s}^{-1}$ , and Harju et al. (1993) with  $0.15\text{ km s}^{-1}$  velocity resolution.

Regarding studies performed with other telescopes, as an example, the  $T_{\text{kin}}$  values calculated from measurements by the Green Bank Telescope (using a  $31''$  beam and  $0.024\text{ km s}^{-1}$  velocity resolution) by Rosolowsky et al. (2008) are generally close to our results, with the  $\text{NH}_3$  column densities and  $T_{\text{kin}}$  both agreeing well (for our targets 81, 82, and 83, which correspond to their sources 123, 121, and 119).

### 3.2. Statistics by Environment

Due to the all-sky selection of the sample, the distances of the targets vary in a wide range, between  $0.11$  and  $10\text{ kpc}$ . Thus, the Effelsberg telescope beam does not cover the same physical scales toward the individual objects, making the tendencies and correlations seen in the calculated physical parameters more difficult to interpret. To make a distinction, we separate the sources into two distance bins. We refer to Kim et al. (2020), who adopted the distances of the sources using estimations based on association with molecular complexes, extinction measurements, and kinetic distance calculations by, e.g., Lombardi et al. (2008), Lada et al. (2009), and Reid et al. (2016). According to Bergin (2007), star-forming dense cores have sizes between  $0.03$  and  $0.2\text{ pc}$ , while clumps show sizes of  $0.3\text{--}3\text{ pc}$ . This means that at distances closer than  $1.5\text{ kpc}$ , the emission detected by the Effelsberg telescope beam of  $37''$  originates from an area similar to core-sized objects, while at distances farther than  $1.5\text{ kpc}$  it comes from an area similar to clump- or cloud-sized objects. Based on the Effelsberg single-pointing observations, we are not able to assess whether the target in the telescope beam is resolved or not; thus, we only make statements of the telescope beam area being clump sized or core sized. We also acknowledge that the nomenclature “core” usually implies a gravitationally bound object, but this cannot be inferred from only the molecular emission data. Further analysis of the SCUBA-2 maps is planned to see whether the objects around the continuum emission peaks are

resolved and to assess the stability of these targets. In this work, “clump-sized” and “core-sized” only refer to size categories. Among the 97 targets, we find 38 core-sized and 59 clump-sized objects.

Table 1 shows the average, median, minimum, and maximum kinetic temperatures and densities of both clump- and core-sized objects in the three environmental (H: high-latitude isolated or small clusters; F: in filaments; C: clusters at the Galactic plane) and two evolutionary groups (S: starless; P: protostellar).

Regarding the environmental groups, high-latitude core-sized objects show the lowest mean ( $12.5 \pm 3.1\text{ K}$ ) kinetic temperatures, while clump-sized objects in filaments show the highest mean ( $16.6 \pm 6.1\text{ K}$ ). The low temperatures far from the Galactic plane may be due to the lack of environmental heating and also might be traced back to the high volume densities (and following efficient cooling) detected there. The mean and minimum  $\text{NH}_3$  column densities are highest in clusters of clump-sized objects at the Galactic plane ( $2.7 \times 10^{15}\text{ cm}^{-2}$  and  $1.2 \times 10^{15}\text{ cm}^{-2}$ ), and the lowest mean and maximum are detected in high-latitude clump-sized targets ( $9.5 \times 10^{14}\text{ cm}^{-2}$  and  $1.2 \times 10^{15}\text{ cm}^{-2}$ ). The highest  $\text{H}_2$  volume densities were found in high-latitude core-sized objects and the lowest in high-latitude clump-sized objects. Generally, clump-sized objects show higher mean temperatures than core-sized ones, on both high and low latitudes, which might be partly caused by the averaging of several (colder and hotter) temperature layers where the telescope beam points at a larger-sized object. Objects in filaments show higher mean temperatures than targets belonging to the isolated or clustered high-latitude sources in the environmental group. Since the majority of filamentary objects are also protostellar, this may be an indication of internal heating or heating by close-by protostars. There are no significant differences between the parameters of the individual targets in filaments, although some filaments are located on higher latitudes while some are closer to the Galactic plane. We find more MVCs at the Galactic plane, which is expected owing to the higher chance of overlapping molecular clouds in the line of sight in this region.

Regarding the evolutionary groups, starless core-sized objects show the lowest kinetic temperatures with a  $12\text{ K}$  mean and a comparatively low,  $16.7\text{ K}$  maximum (due to the lack of internal heating and high volume density) and the highest  $n(\text{H}_2)$  with a  $9.2 \times 10^4\text{ cm}^{-3}$  mean and  $3.6 \times 10^5\text{ cm}^{-3}$  maximum. Clump-sized objects show the highest temperatures (around a  $16\text{ K}$  mean and a  $34\text{--}35\text{ K}$  maximum) and the lowest  $\text{H}_2$  volume densities with a  $1 \times 10^3\text{ cm}^{-3}$  mean and a  $3 \times 10^3\text{ cm}^{-3}$  minimum. Generally, core-sized objects seem to show lower mean, minimum, and maximum kinetic temperatures and higher  $\text{H}_2$  volume densities in both the starless and the protostellar groups, just like among the environmental groups.

While Table 1 shows that the presence of low kinetic temperatures correlates well with high volume densities, the values of  $N(\text{NH}_3)$  vary differently throughout the groups. Among the environmental groups, the highest  $N(\text{NH}_3)$  is observed in a clump-sized object in a filament, but clustered sources at the Galactic plane also show consistently high values. Among the evolutionary groups, starless clump-sized objects seem to show somewhat higher ammonia column densities, but the values show similar ranges in the different groups. Some of these variations might be explained by  $\text{NH}_3$

**Table 1**  
Statistics of the Different Environmental (First Five Rows) and Evolutionary Groups (Last Four Rows)

G	$n$	$T_{\text{kin}}$				$N(\text{NH}_3)$				$n(\text{H}_2)$			
		mean (K)	med (K)	min (K)	max (K)	mean ( $\text{cm}^{-2}$ )	med ( $\text{cm}^{-2}$ )	min ( $\text{cm}^{-2}$ )	max ( $\text{cm}^{-2}$ )	mean ( $\text{cm}^{-3}$ )	med ( $\text{cm}^{-3}$ )	min ( $\text{cm}^{-3}$ )	max ( $\text{cm}^{-3}$ )
C/cl	13	14.9 (2.0)	14.8	11.6	19.9	2.7E+15 (1.4E+15)	2.5E+15	1.2E+15	6.0E+15	8.4E+3 (3.9E+3)	8.3E+3	3.2E+3	1.5E+4
H/cl	8	14.5 (2.4)	13.9	11.8	18.4	9.5E+14 (1.6E+14)	9.0E+14	6.9E+14	1.2E+15	6.7E+3 (2.7E+3)	6.0E+3	3.6E+3	1.2E+4
H/co	27	12.5 (3.1)	11.7	8.0	22.4	1.2E+15 (7.3E+14)	8.4E+14	3.4E+14	3.8E+15	3.5E+4 (7.2E+4)	9.7E+3	5.4E+3	3.6E+5
F/cl	30	16.6 (6.1)	15.6	8.7	35.0	2.3E+15 (2.6E+15)	1.9E+15	6.2E+14	1.5E+16	1.1E+4 (9.9E+3)	8.6E+3	2.9E+3	5.3E+4
F/co	11	15.0 (2.4)	15.8	10.9	17.8	1.3E+15 (5.9E+14)	1.2E+15	4.8E+14	2.6E+15	1.1E+4 (4.3E+3)	9.6E+3	5.2E+3	1.8E+4
S/cl	11	16.1 (6.8)	14.8	8.8	33.9	2.2E+15 (1.6E+15)	2.2E+15	7.3E+14	6.0E+15	1.3E+4 (1.5E+4)	7.7E+3	3.2E+3	5.3E+4
S/co	6	12.0 (3.3)	12.4	8.0	16.7	1.6E+15 (7.4E+14)	2.1E+15	6.3E+14	2.6E+15	9.2E+4 (1.4E+5)	1.7E+4	6.2E+3	3.6E+5
P/cl	40	15.8 (4.3)	15.0	10.1	35.0	2.1E+15 (2.3E+13)	1.8E+15	6.2E+14	1.5E+16	8.9E+3 (5.0E+3)	8.3E+3	2.9E+3	2.5E+4
P/co	32	13.4 (3.1)	13.0	9.0	22.4	1.1E+15 (6.6E+14)	8.4E+14	3.4E+14	3.8E+15	1.6E+4 (1.7E+4)	9.7E+3	5.2E+3	8.4E+4

**Note.** Column (1): categories according to environmental/evolutionary group and spatial size: H—high galactic latitude isolated source or small cluster; C—clusters at the Galactic plane; F—objects in filaments; co—core-sized; cl—clump-sized. Column (2): number of sources in the group. Columns (3)–(6): average, median, minimum, and maximum  $T_{\text{kin}}$ . Columns (7)–(10): average, median, minimum, and maximum  $N(\text{NH}_3)$ . Columns (11)–(14): average, median, minimum, and maximum  $n(\text{H}_2)$ . The numbers in parentheses in Columns (3), (7), and (11) are the standard deviations. The eight targets where no good spectral fit was found (see in Table 3) are missing from this summary.

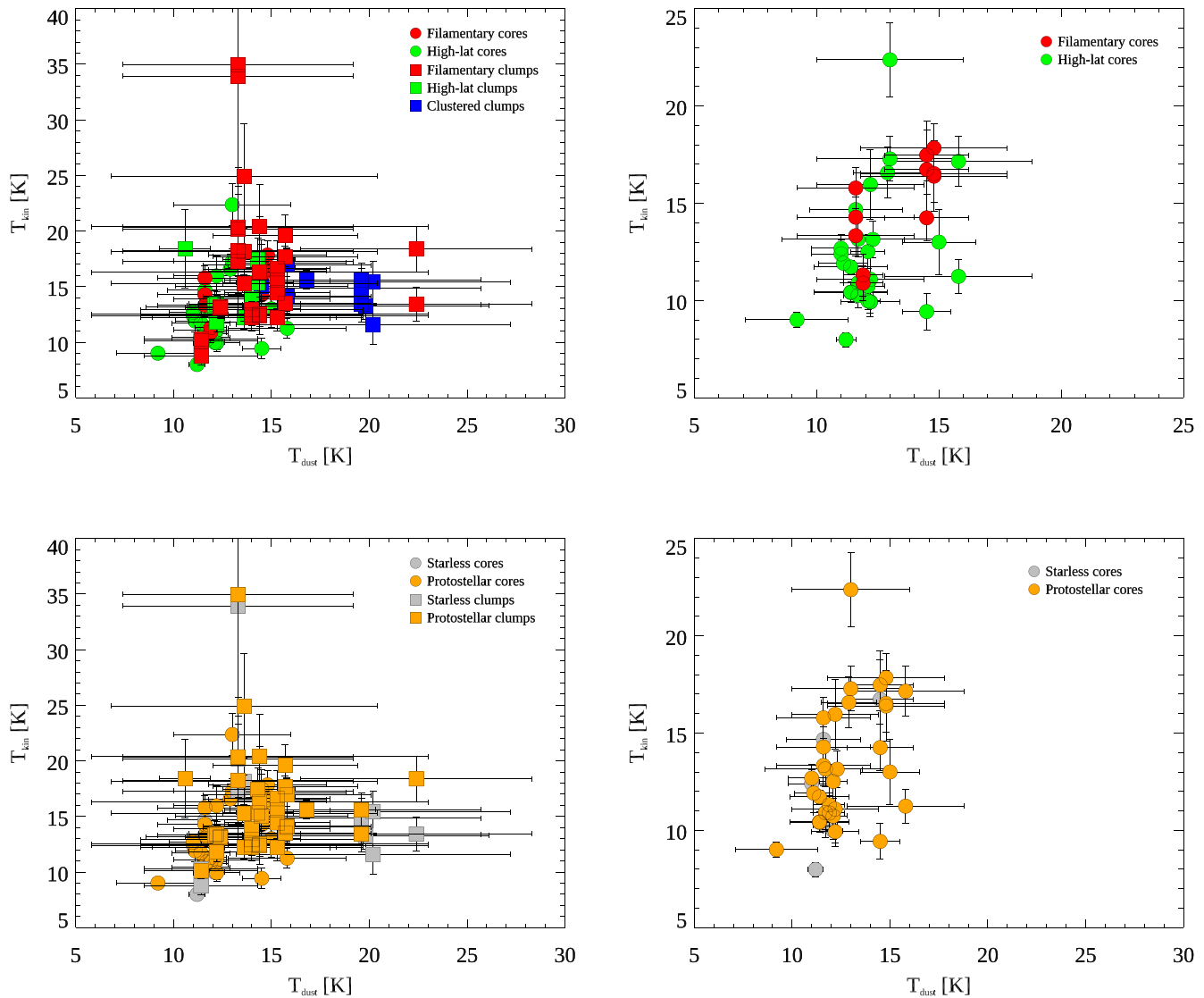


**Figure 2.** Correlation of  $T_{\text{dust}}$  from SCUBA data and  $T_{\text{kin}}$  from  $\text{NH}_3$  data for our SCOPE targets. Correlations are shown for the whole sample (to the right) and separately for only core-sized objects (to the left) and for environmental categories (top row) and evolutionary categories (bottom row) as well.

relative abundance changes in objects of different environments, inside a specific object, or by ammonia freeze-out.

We note that the standard deviations of the mean values are usually large, i.e., the relative errors are 10%–40% for  $T_{\text{kin}}$ , 15%–120% for  $N(\text{NH}_3)$ , and 40%–200% for  $n(\text{H}_2)$ ; thus, the significance of the noted differences is to be handled carefully. We also note that the number of sources in the different categories varies strongly, e.g., no core-sized clustered objects at the Galactic plane were found, but we find four times more protostellar objects than starless ones.

According to the values in Table 4, the objects in different environments show similar velocity dispersions, but high-latitude objects show the lowest and filamentary objects show the highest average  $\sigma_{\text{tot}}$  and  $\sigma_{\text{th}}$ . Protostellar clump-sized objects show high turbulence more often, and starless and protostellar core-sized sources show mostly low turbulence. High turbulence can be caused by protostellar activities such as outflows and spectrally not well-resolved velocity components or line wings. Rotation and other ordered movements of the envelope and circumstellar material can appear as the widening of the detected line as well.

The  $\text{NH}_3(3, 3)$  and  $\text{H}_2\text{O}$  lines were detected in mostly filamentary environments and in protostellar rather than starless sources. From the 25  $\text{NH}_3(3, 3)$  line detections, 14 are toward targets in filaments, 8 are toward clustered objects in the Galactic plane, and 3 are toward high-latitude isolated or small clustered objects. Regarding evolutionary groups, 22  $\text{NH}_3(3, 3)$  detections are associated with protostars and 3 with starless (one in the filamentary environmental group and two in clusters at the Galactic plane). From the 21 water maser detections, 13 were detected in filaments, 1 in clusters at the Galactic plane, and 7 in the high-latitude isolated or small cluster group. All of them are toward protostellar sources. MVCs also mostly appear toward protostellar sources and in filaments, and most of these targets show distances higher than 1.5 kpc. This is easily understood, as at these distances many velocity-coherent parts of a cloud complex can fall into the line of sight and their ammonia emission can be integrated by the telescope beam.

### 3.3. Dependence on Distance and Galactic Position

Figure 2 shows the correlation between the SCUBA-2 submillimeter continuum-based  $T_{\text{dust}}$  values and the hereby

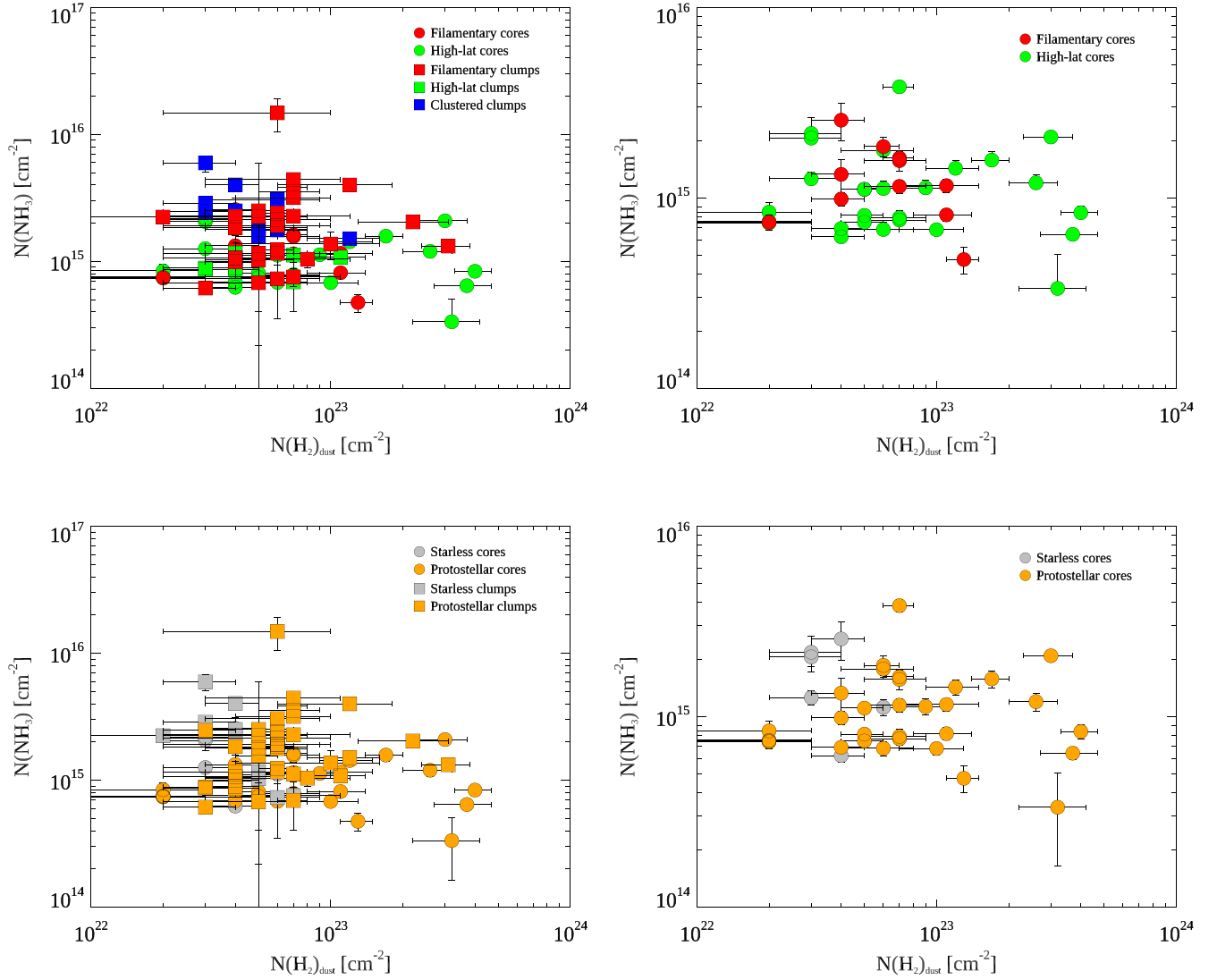


**Figure 3.** Correlation of  $N(\text{H}_2)_{\text{dust}}$  from SCUBA data and  $T_{\text{kin}}$  from  $\text{NH}_3$  data. The symbols are the same as in Figure 2.

derived gas  $T_{\text{kin}}$  kinetic temperatures for the whole sample and separately for only core-sized objects. In case of targets where two velocity components were detected, the average of the two calculated kinetic temperatures is plotted. In the figures showing the whole sample with different symbols for the different environmental and evolutionary categories (top and bottom left) the error bars are generally large, and both values are between 10 and 25 K, with two notable outliers with high  $T_{\text{kin}}$  (around 35 K) and lower  $T_{\text{dust}}$  (around 13 K). Both outliers are clump-sized objects in filaments, one starless and one protostellar (targets 27 and 28), which have two velocity components each. The average of the calculated kinetic temperature from these two components is high for both targets. However, this high temperature comes from the fitting of the weaker velocity component, which is less reliable owing to the relatively high noise. Higher temperatures can be observed in both dust and gas mainly for filamentary and clustered clump-sized objects (red and blue squares). Looking at only core-sized objects, which are thus more comparable physically (top and bottom right), a weak tendency can be observed, with the dust temperatures being somewhat lower than the kinetic temperatures. There is no significant difference in the temperatures of the protostellar and starless groups.

Figure 3 shows the correlation between the SCUBA-2 continuum-based  $N(\text{H}_2)_{\text{dust}}$  hydrogen column densities and the  $N(\text{NH}_3)$  values derived from the line observations. In case of targets where two velocity components were detected, the sum of the two calculated ammonia column densities is plotted. The  $\text{NH}_3$  column densities plotted for the whole sample (top and bottom left) show generally a flat distribution around  $10^{15}$ – $10^{16}$   $\text{cm}^{-2}$  for all values of  $N(\text{H}_2)_{\text{dust}}$  (between  $10^{22}$  and  $10^{24}$   $\text{cm}^{-2}$ ), suggesting an ammonia relative abundance of  $10^{-8}$ – $10^{-6}$  throughout the sample, with some indication of slightly lower ammonia abundances for the highest dust-based  $\text{H}_2$  densities. This could be partly a result of noise in the dust-based column density estimates, but at such high column densities, dust-based  $N(\text{H}_2)$  should underestimate the true  $N(\text{H}_2)$ , so the actual ammonia column density drop might be even larger. Some high-latitude targets (with green) seem to show lower ammonia column densities, while clusters in the Galactic plane (with blue) somewhat higher, with a hint of anticorrelation with dust-based densities. An explanation could be that high-latitude sources are also mostly nearby and thus better-resolved sources, which makes the detection of low abundances more significant because the beam filling factor is higher. In the figures only showing core-sized targets (top and bottom right)



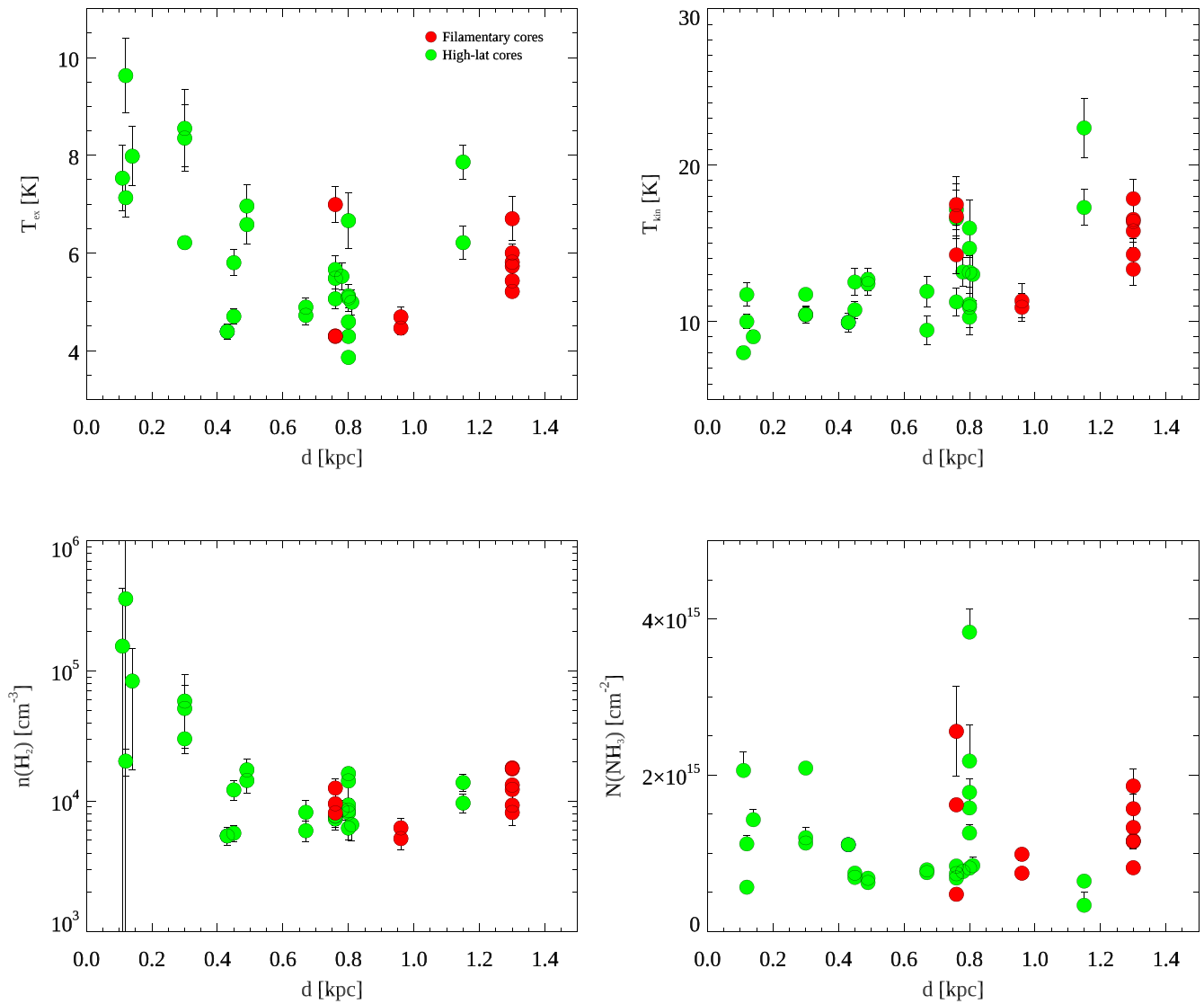


**Figure 4.** Correlation of physical parameters and the distance of the core-sized targets in our sample grouped by environmental categories.

starless objects never show higher  $\text{H}_2$  column densities than  $10^{23} \text{ cm}^{-2}$ , while protostellar objects do. Starless and filamentary core-sized targets show the lowest  $\text{H}_2$  densities.

We examined the correlation between different parameters and distance, galactic latitude, and galactic longitude, restricting the sample to only core-sized targets, i.e., targets at a distance less than 1.5 kpc. Figure 4 shows that  $T_{\text{ex}}$  and  $n(\text{H}_2)$  decrease with distance and reach a plateau around 0.8 kpc, with filamentary core-sized objects (with red) showing lower excitation temperatures and  $\text{H}_2$  volume densities than high-latitude ones (with green). In contrast with this,  $T_{\text{kin}}$  values increase toward larger distances, while the  $N(\text{NH}_3)$  distribution is generally flat with a few outliers around 800 pc and 1.3 kpc. We note that in case of targets where two velocity components were detected, the sum of the two calculated hydrogen volume densities or ammonia column densities and the average of the two excitation or kinetic temperatures are plotted.

The effects of beam dilution might also be observed in the figures showing the dependence of parameters on distance. Assuming externally heated sources where the center of cores or clumps is colder than the outer parts, higher kinetic temperatures for distant sources can be explained by seeing

different core or clump regions depending on distances. This might also explain the higher  $n(\text{H}_2)$  in high-latitude targets, since these mostly contain nearby sources and closer sources have a higher beam filling factor of the high-density gas, while sources in filaments, which are more distant, show only beam-diluted lower density. Mapping observations for the sources would help disentangle the beam dilution effect from real differences in density and temperature.

The parameters of core-sized objects show some systematic changes depending on their galactic latitude and longitude as well. Figure 5 shows that the variation of parameters along the latitude shows lower  $T_{\text{ex}}$  toward lower latitudes, while  $T_{\text{kin}}$  and  $N(\text{NH}_3)$  are higher around the galactic equator. The large errors on the  $n(\text{H}_2)$  values of the cores around  $b = 20^\circ - 40^\circ$  make it difficult to detect a correlation with galactic latitude here. In Figure 6 we see a slight peak in kinetic temperatures and ammonia densities toward  $l = 100^\circ$  and a peak in excitation temperatures at  $b = 2^\circ$  and between  $l = 150^\circ$  and  $200^\circ$ . There is no significant systematic difference between the parameters of starless or protostellar sources or between targets belonging to different environmental categories. Here we only show the figures related to evolutionary categories. The  $T_{\text{kin}}$  peak at

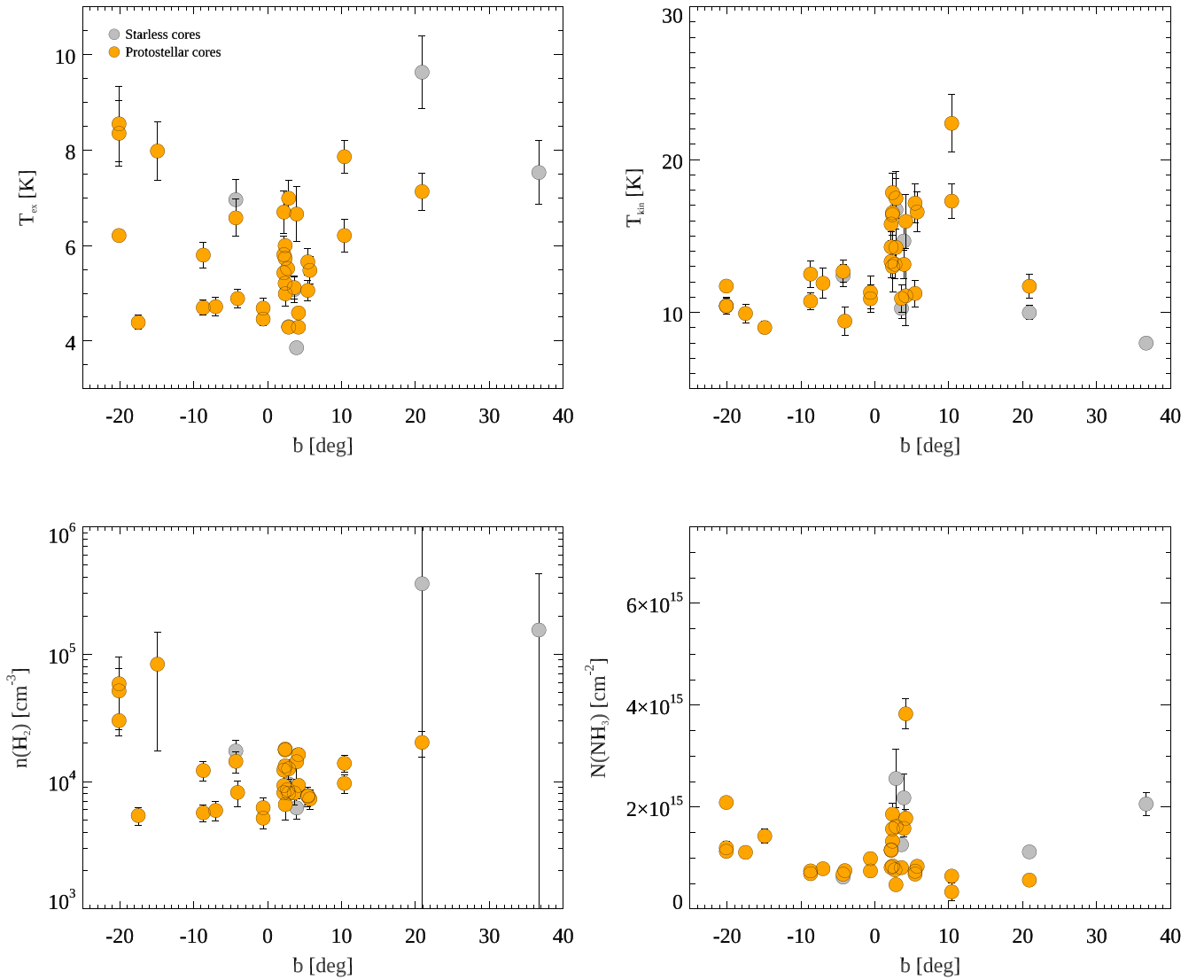


**Figure 5.** Correlation of physical parameters and the galactic latitude of the core-sized targets in our sample grouped by evolutionary categories.

around  $b = 2^\circ$  might be connected to the higher degree of confusion close to the Galactic plane, where parts of several molecular clouds may overlap and contribute to the measured emission in a certain direction. The targets that show the highest  $N(\text{NH}_3)$  are targets 69 and 99. For target 99, the spectrum fitting seems reliable, and even the  $\text{NH}_3(2, 2)$  line seems to show the two velocity components clearly; however, the velocity offset is  $1.6 \text{ km s}^{-1}$ , and thus it is possible that the emission is coming from overlapping but separate objects, increasing the measured column density. For target 69, the secondary velocity component is weaker and more blended and does not appear on the  $(2, 2)$  spectrum; thus, the calculated high  $N(\text{NH}_3)$  is less reliable. These factors contribute to the peak at this galactic latitude and also the peak at  $d = 800 \text{ pc}$  in Figure 4.

In Figure 7 we present the  $\text{H}_2$  volume densities and kinetic temperatures for core-sized targets at similar distances, i.e., farther than 0.5 kpc (and closer than 1.5 kpc from the definition of core-sized objects we used), in order to examine the correlation of these values. This subsample shows  $T_{\text{kin}}$  between 9.4 and 22.4 K, with a mean and median of 14.3 K and a standard deviation of 3.1 K. The  $n(\text{H}_2)$  is between  $5.1 \times 10^3$

and  $1.8 \times 10^4 \text{ cm}^{-3}$ , with a mean of  $9.9 \times 10^3 \text{ cm}^{-3}$ , a standard deviation of  $3.7 \times 10^3 \text{ cm}^{-3}$ , and a median of  $8.6 \times 10^3 \text{ cm}^{-3}$ . In contrast, the cores closer than 0.5 kpc show a mean kinetic temperature of  $10.7 \pm 1.4 \text{ K}$ , a mean  $n(\text{H}_2)$  of  $(6.29 \pm 9.8) \times 10^4 \text{ cm}^{-3}$ , and a median of  $2.03 \times 10^4 \text{ cm}^{-3}$ . This group (with distances less than 0.5 kpc) contains the three targets with the highest  $n(\text{H}_2)$  with the highest error bars.

#### 4. Conclusions

As a pilot study of PGCCs, we have observed three ammonia inversion transitions with the Effelsberg 100 m radio antenna toward 97 cold, dense objects selected from the TOP-SCOPE sample of PGCCs. We classified the sources by eye on the SCUBA-2 images into three environmental groups (high-latitude isolated or clustered targets, objects inside filaments, and clusters close to the Galactic plane) and then, examining their mid-infrared emission seen on WISE and Spitzer maps, into two evolutionary groups (starless and protostellar). The distances of the objects were used to account for their physical size, thus differentiating between close-by core-sized objects and clouds or clumps farther away. Objects closer than 1.5 kpc have physical sizes characteristic of star-forming cores

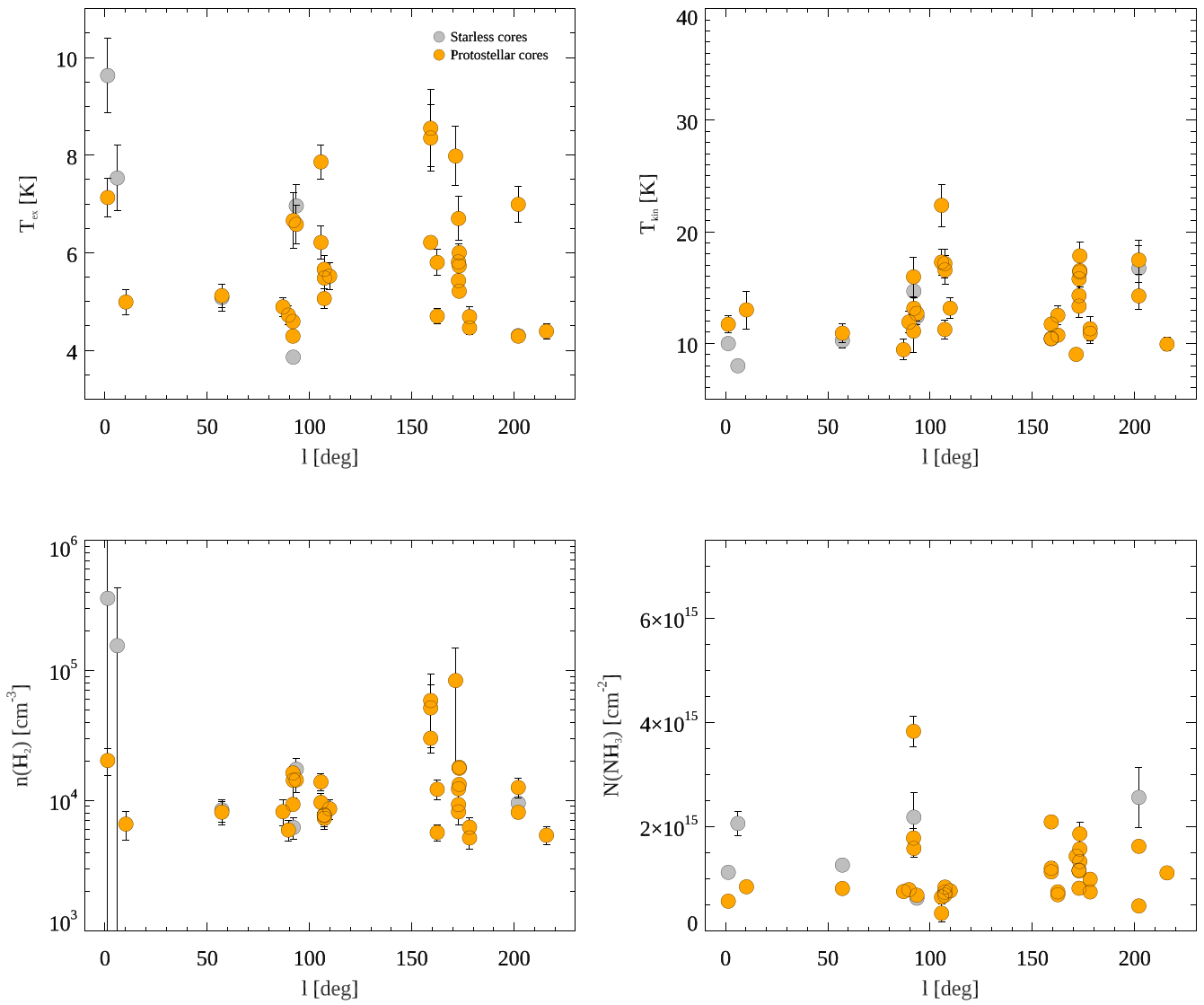


**Figure 6.** Correlation of physical parameters and the galactic longitude of the core-sized targets in our sample grouped by evolutionary categories.

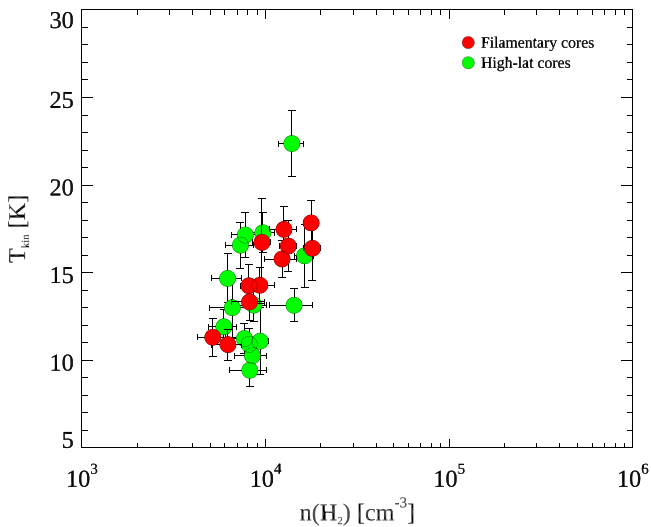


**Figure 7.** Correlation of hydrogen volume density and kinetic temperature for core-sized objects between 0.5 and 1.5 kpc, grouped by environmental categories.

(although their virial stability was not assessed during the current study), while sources farther away may be several cores and clumps in the telescope beam, parsec-scale clumps, or even large molecular clouds.

The detected ammonia lines were used to determine the characteristic temperatures, velocity dispersions,  $\text{NH}_3$  column densities, and  $\text{H}_2$  volume densities of the objects. The rotation and excitation temperatures vary in the range of 7.8–24.2 K and 3.7–9.6 K, respectively, while kinetic temperatures are between 8 and 35 K. The  $\text{NH}_3$  column densities are in the range of  $3.4 \times 10^{14}$ – $1.5 \times 10^{16} \text{ cm}^{-2}$ , the ammonia abundances are between  $10^{-8}$  and  $10^{-6}$ , and the  $\text{H}_2$  volume densities vary between  $2.9 \times 10^3$  and  $3.6 \times 10^5 \text{ cm}^{-3}$ .

We detect the differences between the physical characteristics of sources in different environmental and evolutionary groups, but we note that the values usually have significant relative errors. Most importantly, the ammonia detections seem to allow us to differentiate between warm (possibly internally heated) objects inside filaments and cold, high volume density (sometimes starless) environments on high latitudes. We also detect the anticorrelation between kinetic temperatures and  $\text{H}_2$

volume densities throughout the groups; however, the significance of this has to be evaluated noting the large error bars on these parameters and that beam dilution can affect both values. The variation of  $\text{NH}_3$  column density seems independent from the tendencies of these two parameters. We also note the increasing frequency of MVCs with distance and the detection of water maser and the  $\text{NH}_3(3, 3)$  inversion transition, which is well coupled with protostellar sources associated with filaments. We also examine the correlations between the physical parameters and distance and galactic position. The results of this survey will be used in chemical evolution studies of the TOP-SCOPE collaboration.

This research was supported by the Balaton program 40470VL and the TÉT grant 2017-2.2.5-TÉT-FR-2017-00027. The James Clerk Maxwell telescope is operated by the East Asian Observatory on behalf of the National Astronomical Observatory of Japan; Academia Sinica Institute of Astronomy and Astrophysics; the Korea Astronomy and Space Science Institute; the Operation, Maintenance, and Upgrading Fund for Astronomical Telescopes and Facility Instruments, budgeted from the Ministry of Finance (MOF) of China and administrated by the Chinese Academy of Sciences (CAS); and the National Key R & D Program of China (No. 2017YFA0402700). Additional funding support is provided by the Science and Technology Facilities Council of the United Kingdom and participating universities in the United Kingdom and Canada. The James Clerk Maxwell telescope (JCMT) has historically been operated by the Joint Astronomy Centre on behalf of the Science and Technology Facilities Council of the

United Kingdom, the National Research Council of Canada, and the Netherlands Organization for Scientific Research. Additional funds for the construction of SCUBA-2 were provided by the Canada Foundation for Innovation. This work is based in part on observations made with the Spitzer Space Telescope, which is operated by the Jet Propulsion Laboratory, California Institute of Technology, under a contract with NASA. This publication makes use of data products from the Wide-field Infrared Survey Explorer, which is a joint project of the University of California, Los Angeles, and the Jet Propulsion Laboratory/California Institute of Technology, funded by the National Aeronautics and Space Administration. This research has made use of the SIMBAD database, operated at CDS, Strasbourg, France.

## Appendix A Tables

The observed targets and their associated PGCCs, coordinates, distances, environmental categories, and references to previous publications presenting ammonia or water maser observations toward them are in Table 2. Table 3 lists the results from the Gaussian and HFS fitting to the  $\text{NH}_3(1, 1)$  and  $(2, 2)$  lines detected toward the targets and whether the targets are associated with  $\text{NH}_3(3, 3)$  line and water maser detections. Using the results from the line fitting, physical parameters had been calculated for toward the targets, and these parameters are listed in Table 4, together with the evolutionary and environmental categories the targets were sorted into.

**Table 2**  
Observed Targets

<i>N</i>	PGCC ID	SCOPE ID	R.A. (J2000) (hh:mm:ss)	Decl. (J2000) (dd:mm:ss)	Distance (kpc)	Env.	NH <sub>3</sub>	H <sub>2</sub> O
1	G1.40+20.93	G001.3+20.9A1.01	16:34:29.28	−15:47:02.4	0.12	H	1, 2	...
2		G001.3+20.9A1.02	16:34:35.28	−15:46:55.2	0.12	H	1, 3	23
3	...	G005.91−01.00.01	18:02:51.36	−24:20:06.0	2.25	F	...	...
4		G005.91−01.00.02	18:02:58.08	−24:21:25.2	2.25	F	...	...
5		G005.91−01.00.03	18:02:50.16	−24:22:26.4	2.25	F	...	...
6		G005.91−01.00.04	18:02:42.00	−24:19:04.8	2.25	F	...	...
7		G005.91−01.00.05	18:02:53.04	−24:21:43.2	2.25	F	...	...
8	G6.04+36.77	G006.0+36.7A1.01	15:54:08.64	−02:52:40.8	0.11	H	1, 4	...
9	G10.20+2.40	G10.20+2.40.01	17:59:15.36	−18:56:42.0	0.81	H	...	...
10	G14.14−0.55	G14.14−0.55.01	18:18:13.20	−16:57:21.6	1.85	F	5, 6*, 7	24
11		G14.14−0.55.02	18:18:12.72	−16:49:33.6	1.85	F	5, 7, 8, 9*	25

**Note.** Column (1): identification number. Column (2): name of the associated PGCC. Column (3): identification in the SCOPE survey. Columns (4) and (5): central equatorial coordinates of the target. Column (6): distance based on Kim et al. (2020) and references therein. Column (7): environment: H—high-latitude isolated or small clusters; F—in filament; C—clusters at the Galactic plane. Column (8): references to previous publications reporting on NH<sub>3</sub> observations that include the target. (1) Jijina et al. (1999); (2) Benson & Myers (1989); (3) Anglada et al. (1989); (4) Ungerechts et al. (1980); (5) Camarata et al. (2015); (6) Svoboda et al. (2016); (7) Wienen et al. (2012); (8) Anglada et al. (1996); (9) Longmore et al. (2017); (10) Tang et al. (2017); (11) Rygl et al. (2010); (12) Urquhart et al. (2014); (13) Urquhart et al. (2011); (14) Chira et al. (2013); (15) Keown et al. (2019); (16) Torrelles et al. (1983); (17) Güsten & Marcaide (1986); (18) Tafalla et al. (1993); (19) Molinari et al. (1996); (20) Harju et al. (1993); (21) Rosolowsky et al. (2008); (22) Codella et al. (1994). Column (9): references to previous publications reporting on H<sub>2</sub>O maser observations that include the target. (23) Han et al. (1995); (24) Svoboda et al. (2016); (25) Palagi et al. (1993); (26) Walsh et al. (2011); (27) Codella et al. (1994); (28) Wang et al. (2006); (29) Sunada et al. (2007); (30) Gómez et al. (2006); (31) Valdettaro et al. (2001); (32) Urquhart et al. (2011). The reference numbers in both Columns (8) and (9) are marked with a star if the position of the previous measurement is in the 1′–2′ radius area around our target, thus considered as “associated,” but outside the 37″ Effelsberg beam. Note: during data reduction, targets 63, 64, and 67 were found to be duplicates of targets 59, 60, and 66 and thus were excluded from further analysis.

(This table is available in its entirety in machine-readable form.)

**Table 3**  
Line Fit Results

<i>N</i>	<i>L</i>	$T_{\text{MB}}(1, 1)$ (K)	$v_{\text{LSR}}(1, 1)_{\text{HFS}}$ (K)	$\Delta v_{\text{HFS}}(1, 1)$ (km s <sup>−1</sup> )	$\Delta v_{\text{g}}(1, 1)$ (km s <sup>−1</sup> )	$\tau_m(1, 1)$	$T_{\text{MB}}(2, 2)$ (K)	$\sigma_{\text{th}}$ (km s <sup>−1</sup> )	$\sigma_{\text{tu}}$ (km s <sup>−1</sup> )	(3, 3)	H <sub>2</sub> O
1	1	3.97 (0.35)	0.505 (0.003)	0.436 (0.007)	0.790 (0.029)	2.37 (0.11)	0.77 (0.12)	0.076 (0.019)	0.169 (0.001)	Y	...
2	1	6.87 (0.76)	0.784 (0.001)	0.273 (0.002)	0.718 (0.033)	6.62 (0.12)	1.81 (0.11)	0.070 (0.015)	0.093 (0.001)	...	...
3		no good fit found							...	...	...
4		no good fit found							...	...	...
5		no good fit found							...	Y	...
6		no good fit found							...	...	...
7		no good fit found							...	...	...
8	1	4.78 (0.67)	2.437 (0.001)	0.236 (0.002)	0.737 (0.041)	10.79 (0.22)	0.81 (0.09)	0.063 (0.013)	0.078 (0.001)	...	...
9	1	1.80 (0.21)	5.939 (0.010)	0.871 (0.026)	1.118 (0.053)	1.62 (0.12)	0.38 (0.13)	0.080 (0.029)	0.361 (0.002)	...	...
10	1	3.99 (0.09)	19.496 (0.021)	1.640 (0.033)	1.831 (0.025)	1.14 (0.02)	1.69 (0.10)			Y	...
	2	1.60 (0.09)	21.458 (0.045)	1.331 (0.077)	1.797 (0.063)	1.24 (0.19)	0.48 (0.10)				...

**Note.** Column (1): identification number. Column (2): number of detected NH<sub>3</sub>(1, 1) velocity components. Column (3): NH<sub>3</sub>(1, 1) main-group main-beam brightness. Column (4): NH<sub>3</sub>(1, 1) LSR velocity from HFS fitting. Column (5): NH<sub>3</sub>(1, 1) HFS line width. Column (6): NH<sub>3</sub>(1, 1) main-group Gaussian line width. Column (7): NH<sub>3</sub>(1, 1) main-group opacity. Column (8): NH<sub>3</sub>(2, 2) main-beam brightness. Column (9): thermal velocity dispersion. Column (10): turbulent velocity dispersion. Columns (11) and (12): presence of NH<sub>3</sub>(3, 3) or H<sub>2</sub>O maser emission.

(This table is available in its entirety in machine-readable form.)

**Table 4**  
Physical Parameters of the Targets

$N$	$L$	$T_{\text{rot}}$ (K)	$T_{\text{ex}}$ (K)	$T_{\text{kin}}$ (K)	$N(\text{NH}_3)$ ( $\text{cm}^{-2}$ )	$n(\text{H}_2)$ ( $\text{cm}^{-3}$ )	Evol. Group	Env. Group
1	1	$11.01 \pm 0.57$	$7.13 \pm 0.39$	$11.71 \pm 0.76$	$5.66\text{E}+14 \pm 4.58\text{E}+13$	$2.03\text{E}+04 \pm 4.63\text{E}+03$	P	H
2	1	$9.56 \pm 0.33$	$9.63 \pm 0.76$	$9.98 \pm 0.46$	$1.12\text{E}+15 \pm 1.10\text{E}+14$	$3.58\text{E}+05 \pm 9.40\text{E}+05$	S	H
3	no good fit found						P	F
4	no good fit found						P	F
5	no good fit found						P	F
6	no good fit found						P	F
7	no good fit found						P	F
8	1	$7.79 \pm 0.29$	$7.53 \pm 0.67$	$7.99 \pm 0.37$	$2.06\text{E}+15 \pm 2.32\text{E}+14$	$1.55\text{E}+05 \pm 2.75\text{E}+05$	S	H
9	1	$12.04 \pm 1.39$	$4.99 \pm 0.26$	$13.00 \pm 1.69$	$8.43\text{E}+14 \pm 1.05\text{E}+14$	$6.59\text{E}+03 \pm 1.61\text{E}+03$	P	
10	1	$16.77 \pm 0.51$	$8.63 \pm 0.15$	$19.52 \pm 0.93$	$8.25\text{E}+14 \pm 2.41\text{E}+13$	$1.88\text{E}+04 \pm 1.62\text{E}+03$	P	F
	2	$14.22 \pm 1.22$	$5.00 \pm 0.12$	$15.86 \pm 1.62$	$1.21\text{E}+15 \pm 1.96\text{E}+14$	$5.89\text{E}+03 \pm 9.09\text{E}+02$		

**Note.** Column (1): identification number. Column (2): number of detected  $\text{NH}_3(1, 1)$  velocity components. Column (3): rotation temperature from (1, 1) and (2, 2) levels. Column (4): excitation temperature of the  $\text{NH}_3(1, 1)$  transition. Column (5): kinetic temperature. Column (6):  $\text{NH}_3$  column density. Column (7):  $\text{H}_2$  volume density. Column (8): result of YSO association: P—protostellar; S—starless. Column (9): environmental category of the target: H—high-latitude isolated or small clusters; F—in filament; C—clusters at the Galactic plane (the same as Column (9) in Table 2).

(This table is available in its entirety in machine-readable form.)

## Appendix B Figures

The detected water maser spectra are plotted in Figure 8. The infrared and submillimeter environment measured by Spitzer

and WISE is plotted in Figure 9, together with the PGCC ellipses. The detected  $\text{NH}_3(1, 1)$ , (2, 2), and (3, 3) lines toward the targets are plotted in Figure 10.

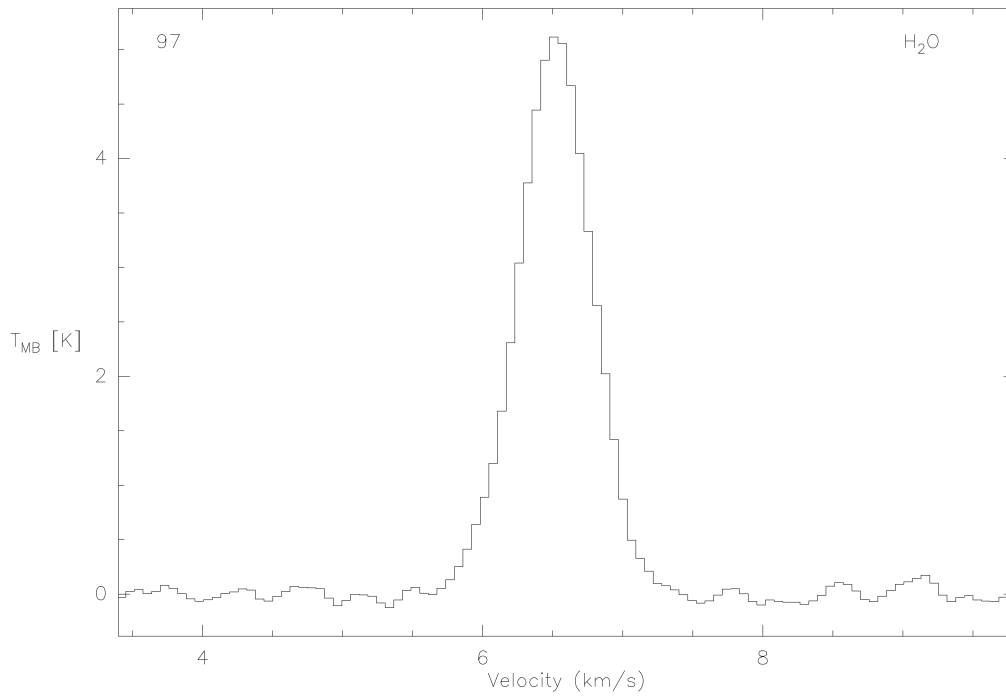


**Figure 8.** Spectra of the water maser detections in our sample. The numbers in the upper-left corner of each panel correspond to the target number in Table 2. The spectrum of target 97 is shown as an example.

(The complete figure set (21 images) is available.)

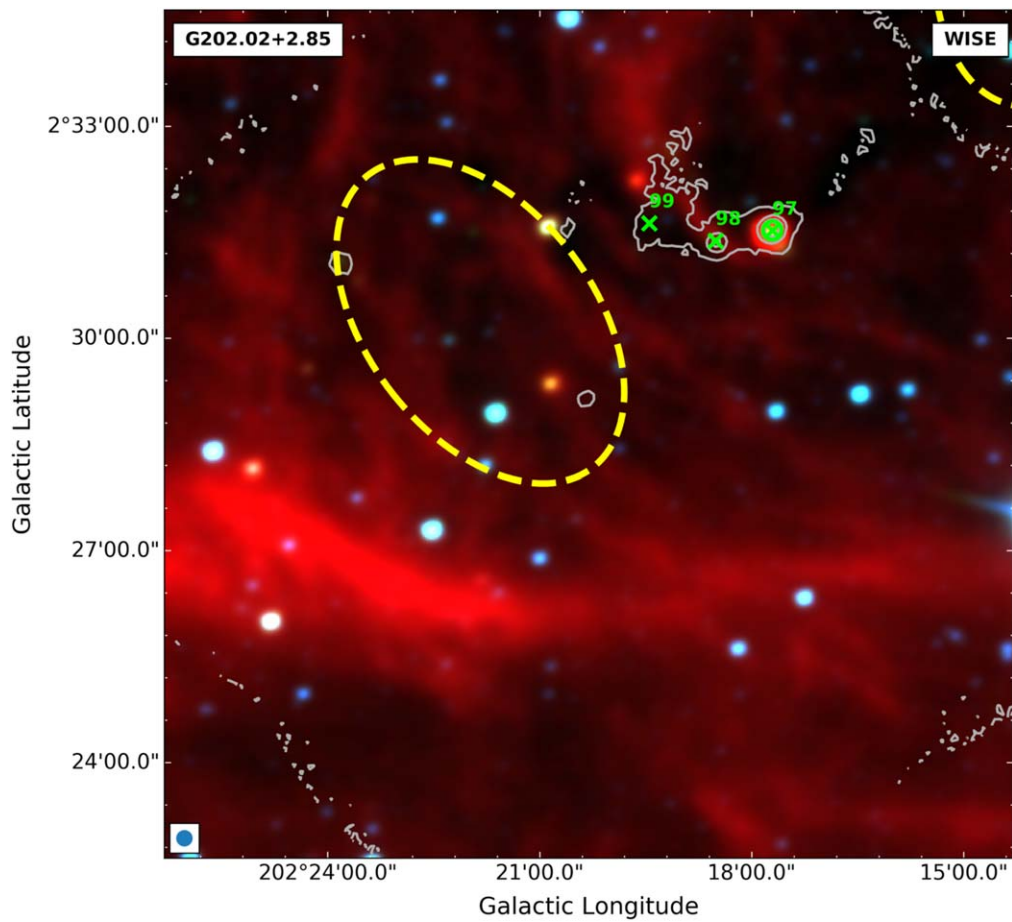


**Figure 9.** The infrared and submillimeter environment of our targets. The color scale shows the Spitzer or WISE RGB maps of the area (blue for the shortest, green for the intermediate, and red for the longest wavelength). Gray contours are from the SCUBA-2 850  $\mu\text{m}$  map (at 10%, 30%, 50%, and 70% of the maximum value), yellow ellipses show the PGCCs, green crosses show the locations of the SCOPE clumps, and green circles mark the targets where water maser emission was also detected. The SCUBA-2 beam of 14'' is plotted in the lower left corner of each panel. The environment of PGCC G202.03+2.85 is shown as an example.

(The complete figure set (46 images) is available.)



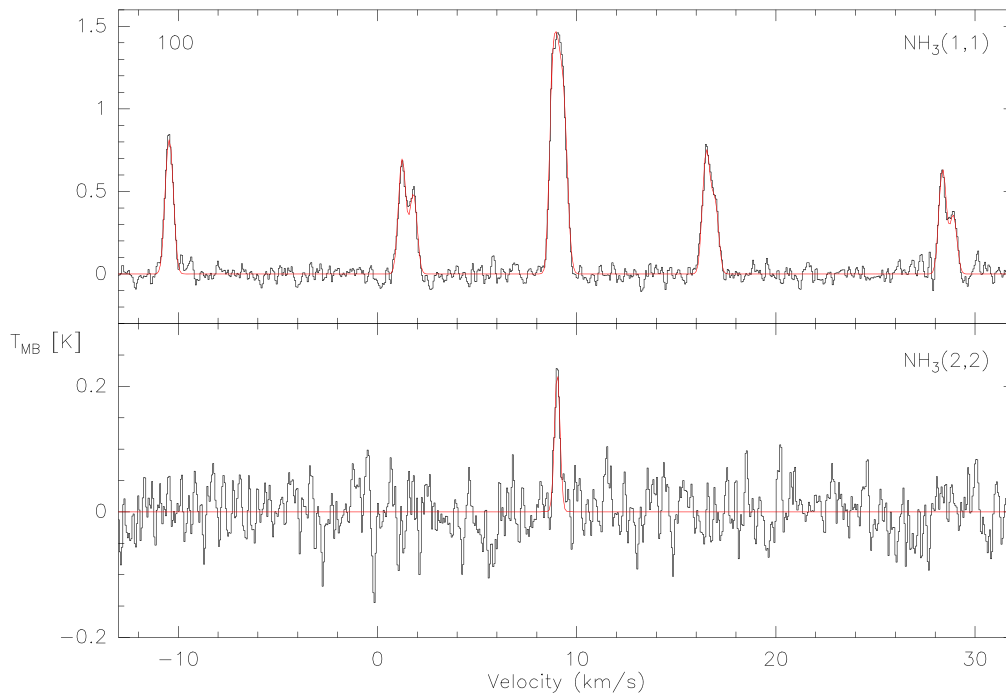


**Figure 10.**  $\text{NH}_3(1, 1)$ ,  $(2, 2)$ , and  $(3, 3)$  spectra toward our targets. Red lines show the fitted HFS and Gaussian functions to the lines. The numbers in the upper left corner of each panel correspond to the target number in Table 2. The  $\text{NH}_3$  spectra of target 100 are shown as an example.

(The complete figure set (97 images) is available.)

### ORCID iDs

O. Fehér <https://orcid.org/0000-0003-3453-4775>  
 Alex Kraus <https://orcid.org/0000-0002-4184-9372>  
 Tie Liu <https://orcid.org/0000-0002-5286-2564>  
 Ken'ichi Tatematsu <https://orcid.org/0000-0002-8149-8546>  
 David J. Eden <https://orcid.org/0000-0002-5881-3229>  
 Naomi Hirano <https://orcid.org/0000-0001-9304-7884>  
 Mika Juvela <https://orcid.org/0000-0002-5809-4834>  
 Kee-Tae Kim <https://orcid.org/0000-0003-2412-7092>  
 Di Li <https://orcid.org/0000-0003-3010-7661>  
 Sheng-Yuan Liu <https://orcid.org/0000-0003-4603-7119>  
 Yuefang Wu <https://orcid.org/0000-0002-5076-7520>

### References

- Anglada, G., Estalella, R., Pastor, J., et al. 1996, *ApJ*, 463, 205  
 Anglada, G., Rodríguez, L. F., Torrelles, J. M., et al. 1989, *ApJ*, 341, 208  
 Benson, P. J., & Myers, P. C. 1989, *ApJS*, 71, 89  
 Bergin, Edwin A., & Tafalla, Mario 2007, *ARA&A*, 45, 1  
 Camarata, M. A., Jackson, J. M., & Chambers, E. 2015, *ApJ*, 806, 74  
 Chira, R.-A., Beuther, H., Linz, H., et al. 2013, *A&A*, 552, A40  
 Codella, C., Felli, M., Natale, V., et al. 1994, *A&A*, 291, 261  
 Danby, G., Flower, D. R., Valiron, P., et al. 1988, *MNRAS*, 235, 229  
 Eden, D. J., Liu, Tie, Kim, K.-T., et al. 2019, *MNRAS*, 485, 2895  
 Fehér, O., Tóth, L. V., Ward-Thompson, D., et al. 2016, *A&A*, 590, A75  
 Gómez, J. F., de Gregorio-Monsalvo, I., Suárez, O., & Kuiper, T. B. H. 2006, *AJ*, 132, 1322  
 Güsten, R., & Marcaide, J. M. 1986, *A&A*, 164, 342  
 Han, F., Mao, R. Q., Lei, C. M., et al. 1995, *PPMTO*, 14, 184  
 Harju, J., Walmsley, C. M., & Wouterloot, J. G. A. 1993, *A&AS*, 98, 51  
 Ho, P. T. P., & Townes, C. H. 1983, *ARA&A*, 21, 239  
 Jijina, J., Myers, P. C., & Adams, Fred C. 1999, *ApJS*, 125, 161  
 Juvela, M., Demyk, K., Doi, Y., et al. 2015a, *A&A*, 584, A94  
 Juvela, M., Harju, J., Ysard, N., & Lunttila, T. 2012a, *A&A*, 538, A133  
 Juvela, M., Ristorcelli, I., Marshall, D. J., et al. 2015b, *A&A*, 584, A93  
 Juvela, M., Ristorcelli, I., Pagani, L., et al. 2012b, *A&A*, 541, A12  
 Keown, J., Di Francesco, J., Rosolowsky, E., et al. 2019, *ApJ*, 884, 4  
 Kim, G., Tatematsu, K., Liu, T., et al. 2020, *ApJS*, 249, 33  
 Lada, C. J., Lombardi, M., & Alves, J. F. 2009, *ApJ*, 703, 52  
 Liu, T., Kim, K.-T., Juvela, M., et al. 2018, *ApJS*, 234, 28  
 Liu, T., Zhang, Q., Kim, K.-T., et al. 2016, *ApJS*, 222, 7  
 Lombardi, M., Lada, C. J., & Alves, J. 2008, *A&A*, 489, 143  
 Longmore, S. N., Walsh, A. J., Purcell, C. R., et al. 2017, *MNRAS*, 470, 1462  
 Meng, F., Wu, Y., & Liu, T. 2013, *ApJS*, 209, 37  
 Molinari, S., Brand, J., Cesaroni, R., & Palla, F. 1996, *A&A*, 308, 573  
 Montillaud, J., Juvela, M., Rivera-Ingraham, A., et al. 2015, *A&A*, 584, A92  
 Palagi, F., Cesaroni, R., Comoretto, G., et al. 1993, *A&AS*, 101, 153  
 Planck Collaboration XXXVIII 2016, *A&A*, 594, A28  
 Reid, M. J., Dame, T. M., Menten, K. M., & Brunthaler, A. 2016, *ApJ*, 823, 77  
 Rosolowsky, E. W., Pineda, J. E., Foster, J. B., et al. 2008, *ApJS*, 175, 509  
 Rygl, K. L. J., Wyrowski, F., Schuller, F., & Menten, K. M. 2010, *A&A*, 515, A42  
 Sunada, K., Nakazato, T., Ikeda, N., et al. 2007, *PASJ*, 59, 1185  
 Svoboda, B. E., Shirley, Y. L., Battersby, C., et al. 2016, *ApJ*, 822, 59  
 Tafalla, M., Bachiller, R., & Martín-Pintado, J. 1993, *ApJ*, 403, 175  
 Tafalla, M., Myers, P. C., Caselli, P., & Walmsley, C. M. 2004, *A&A*, 416, 191  
 Tang, X. D., Henkel, C., Menten, K. M., et al. 2017, *A&A*, 598, A30  
 Tatematsu, K., Liu, T., Kim, G., et al. 2020, *ApJ*, 895, 119  
 Tatematsu, K., Liu, T., Ohashi, S., et al. 2017, *ApJS*, 228, 12  
 Torrelles, J. M., Rodríguez, L. F., Canto, J., et al. 1983, *ApJ*, 274, 214  
 Tóth, L. V., Haas, M., Lemke, D., Mattila, K., & Onishi, T. 2004, *A&A*, 420, 533  
 Ungerechts, H., Walmsley, C. M., & Winnewisser, G. 1980, *A&A*, 88, 259  
 Urquhart, J. S., Figura, C. C., Moore, T. J. T., et al. 2014, *MNRAS*, 437, 1791  
 Urquhart, J. S., Morgan, L. K., Figura, C. C., et al. 2011, *MNRAS*, 418, 1689  
 Valdettaro, R., Palla, F., Brand, J., et al. 2001, *A&A*, 368, 845  
 Walsh, A. J., Breen, S. L., Britton, T., et al. 2011, *MNRAS*, 416, 1764  
 Wang, Y., Zhang, Q., Rathborne, J. M., et al. 2006, *ApJ*, 651, L125  
 Wenger, M., Ochsenein, F., Egret, D., et al. 2000, *A&AS*, 143, 9  
 Werner, M. W., Roellig, T. L., Low, F. J., et al. 2004, *ApJS*, 154, 1  
 Wielen, M., Wyrowski, F., Schuller, F., et al. 2012, *A&A*, 544, A146  
 Wright, E. L., Eisenhardt, P. R. M., Mainzer, A. K., et al. 2010, *AJ*, 140, 1868  
 Wu, Y., Liu, T., Meng, F., et al. 2012, *ApJ*, 756, 76  
 Zijlstra, A., Van Hoof, P. A. M., & Perley, R. A. 2008, *ApJ*, 681, 1296